Revision 2

Experimental melt inclusion homogenization in a hydrothermal diamond-anvil cell: a comparison with homogenization at one atmosphere

Shenghu Li[1, 2], Jiankang Li[3*], and I-Ming Chou[4]

[1] Shandong Institute of Geological Sciences, Key Laboratory of Gold Mineralization Processes and Resources Utilization Subordinated to the Ministry of Natural Resources, Key Laboratory of Metallogenic Geological Processes and Resources Utilization in Shandong Province, Jinan 250013, China

[2] School of Earth Sciences and Resources, China University of Geosciences, Beijing 100083, China

[3] MNR Key Laboratory of Metallogeny and Mineral Assessment, Institute of Mineral Resources, Chinese Academy of Geological Sciences, Beijing 100037, China

[4] CAS Key Laboratory of Experimental Study under Deep-sea Extreme Conditions, Institute of Deep-sea Science and Engineering, Chinese Academy of Sciences, Sanya, Hainan 572000, China

[*]Corresponding author: Jiankang Li

E-mail: Li9968@126.com

ABSTRACT

Melt inclusion (MI) homogenization experiments are essential for determining the pressure–volume–temperature–composition (*P–V–T–X*) parameters of magma systems. The hydrothermal diamond-anvil cell (HDAC) is currently the only equipment that can exert external pressure on MIs while allowing *in situ* observation of MI phase changes during heating. The HDAC's pressure potentially prevents the MI diffusion that, under heating at one atmosphere, produces artificially elevated measurements of phase transition temperatures. It is important to compare the phase transition temperatures measured using HDAC at elevated external pressure with those obtained using conventional equipment at one atmosphere. Such a comparison not only helps assess the reliability of HDAC phase transition temperatures but also helps determine phase transition temperatures that are naturally occurring in MI during the natural history of cooling.

In this study, we homogenized MIs hosted in quartz from the granitic porphyry in the Yixingzhai Au deposit, China, using HDAC at an elevated pressure of ~(140–230) MPa. We compared our experimental results with published data measured using a Linkam TS1500 stage at one atmosphere. The experiments show that the initial melting temperature (T_{IniM}), total melting temperature (T_{TotM}), and total homogenization temperature (T_{hTot}) of the MIs are 695 ± 20 °C, 780 ± 15 °C, and 833 ± 17 °C respectively. These phase transition temperatures are as much as 374 °C lower than the corresponding values measured at one atmosphere using the

Linkam stage. Moreover, the temperatures measured using HDAC agree with actual values estimated using the linear extrapolation method based on correlations of MI size with phase transition temperatures measured using the Linkam stage. Based on the experimental HDAC results, we estimate that MIs in the Yixingzhai Au deposit were trapped at ~140 Ma and contained ~2 wt% H_2O. These figures are consistent with previously estimated emplacement pressures and H_2O contents of granitic magmas in granitic porphyry-type Cu–Au deposits. These features demonstrate that MI-homogenization experiments using HDAC at suitably elevated pressures can yield reliable naturally occurring phase transition temperatures in MI during the melt cooling process.

Keywords: melt inclusions, hydrothermal diamond-anvil cell, Linkam heating stage, homogenization experiment, H_2O content

INTRODUCTION

Melt inclusions (MIs) are naturally occurring drops of magma trapped among crystallizing magmatic mineral grains (e.g., olivine, pyroxene, feldspar, hornblende, quartz, and garnet). MIs occur in both eruptive and intrusive rocks (Halter et al. 2004; Lowenstern 1995). Once trapped at high pressure–temperature (*P*–*T*) conditions, MIs are sealed in the relatively incompressible host minerals, preserving physicochemical information about the surrounding magma medium during the crystallization of the

64 host minerals (Smirnov et al. 2003; Webster and Thomas 2006). Post-entrapment,
65 crystallization or devitrification can occur when the *P–T* of the ambient environment
66 decrease, producing compositional heterogeneity in any given inclusion. Therefore, in
67 order to determine the pressure–volume–temperature–composition (*P–V–T–X*)
68 evolutionary trajectories of MIs during the crystallization of a melt, as well as MI
69 compositions, MIs must be experimentally homogenized for analysis of various kinds:
70 electron microprobe analysis, secondary ion mass spectrometer, and Fourier-transform
71 infrared spectroscopy (Roedder 1979; Schiano 2003; Thomas 2000).

72 Several heating techniques have been used to successfully homogenize MI at one
73 atmosphere pressure, either in a microscope-mounted stage (e.g., Linkam stage;
74 Esposito et al. 2012; Fedele et al. 2003; Lowenstern 1994; Magakyan et al. 1993;
75 Reyf 1997) or tube furnace (Raia et al. 2000; Stockstill et al. 2005; Thomas and
76 Webster 2000; Webster et al. 1997; Yang and Bodnar 1994). These heating techniques
77 work well for MI with low concentrations of volatiles, such as MIs hosted in volcanic
78 rocks (Bodnar and Student, 2006; Cannatelli et al. 2016). Using these techniques, the
79 measured homogenization temperatures (T_hs) and behavior are affected by the heating
80 rate, inclusion size, and volatiles content (Audétat and Lowenstern 2014; Bodnar and
81 Student, 2006; Danyushevsky et al. 2002; Lowenstern 1994; Qin et al. 1992; Student
82 and Bodnar 1999, 2004; Thomas 1994). For example, large inclusion size and long
83 heating time will increase the likelihood that the inclusion composition (e.g., H_2O)
84 change as a result of component diffusion out of (or into) the inclusion, and then

85 increase the T_h deviation from the correct value (Massare et al. 2002; Severs et al.
86 2007; Thomas 1994). Consequently, the kinetic experiments of volatile diffusion
87 inside MIs are required to assess the T_hs of MIs heated at one atmosphere pressure, as
88 described by Danyushevsky et al (2002) and Thomas (1994). Moreover, if the MIs
89 contain significant amounts of volatiles (e.g., H_2O), such techniques are hard to
90 homogenize MIs as they are commonly decrepitated before T_h is reached, owing to
91 the high internal pressures generated during heating (Audétat and Lowenstern 2014;
92 Bodnar and Student 2006). Therefore, MIs enriched with volatiles were usually
93 heated under an elevated confining pressure with high-pressure (cold-sealed or
94 internally heated) vessels (Anderson et al. 2000; Severs et al. 2007; Skirius et al. 1990;
95 Student and Bodnar 2004; Thomas et al. 2003), or in a piston cylinder apparatus
96 (Bartoli et al. 2011; Cesare et al. 2011; Ferrero et al. 2012). Using the pressurized
97 equipment, MIs are heated incrementally and then quenched after each heating step
98 for observing and obtaining the stable phase transition temperatures (Thomas and
99 Davidson 2016b). This technology does not allow MIs to be monitored in *situ* during
100 heating, the phase transition temperatures could be measured with some errors
101 (Student and Bodnar 2004); it could also cause MIs to be overheated and then
102 increase the chance of MI decrepitation in some cases, especially for the larger
103 inclusions (greater than approximately 30–50 μm) (Bodnar and Student 2006).

104 HDAC was designed to study the properties of fluids at pressures up to 2.5 GPa
105 and temperatures ranging from −190 to 1200 °C (Bassett et al. 1993; Li et al. 2016,

2020). Thomas et al. (2006) suggested HDAC be used in MI-homogenization experiments, to provide the opportunity to observe phase transitions *in situ* during MI heating under elevated appropriate external pressures. Later, Li and Li (2014) and Li and Chou (2017) established the MI-homogenization experimental method using HDAC. However, more experiments are essential for evaluating whether the phase transition temperatures observed using HDAC experiments reflect those naturally occurring in MIs during the natural history of cooling. Therefore, in this study, we used HDAC to homogenize MIs in quartz from the Yixingzhai granite porphyry-type Au deposit, Shanxi Province, China, in order to compare the homogenization results of MIs heated in a Linkam heating stage at one atmosphere as performed by Wang (2014). The results of this study illustrate the evident effect of the external pressure on the measured phase transition temperature within a given MI while demonstrating the reliability of phase transition temperatures measured using HDAC.

FEATURES OF MELT INCLUSIONS IN THE YIXINZHAI GOLD DEPOSIT

The Yixingzhai Au deposit is a representative porphyry-type gold deposit in northern Shanxi Province, China, located at the intersection of the Taihang and Yanshan orogenic belts, on the northern margin of the North China Block. The Yixingzhai Au deposit consists mainly of quartz porphyry and its associated cryptoexplosive breccia. Among these rocks, quartz porphyry is the main metallogenic rock, bearing a typical porphyritic texture (Wang 2014). In this study, we selected MIs hosted in the quartz phenocrysts of quartz porphyry from the Yixingzhai

Au deposit for use in MI-homogenization experiments.

In the quartz porphyry, quartz occurs as 2–3 mm phenocrysts of subhedral shape (Fig. 1), hosting numerous MIs (Fig. 2). These MIs exhibit the characteristics of primary inclusions: typically elliptical in shape, 10–25 μm in size, occurring in isolation or in MI assemblages (MIAs) consisting of MIs with uniform shape and composition (Fig. 2a). The MIs are commonly dark to opaque in transmitted light, owing to the presence of abundant crystallites formed during MI devitrification. As a result, aqueous phases were too obscure to be observed by optical microscopy at room temperature. The MIs are composed primarily of feldspar and quartz as identified by Raman spectroscopy (Wang 2014). Additionally, some MIs coexist with CO_2–H_2O fluid inclusions (Fig. 2b).

EXPERIMENTAL METHODS

In the homogenization experiments of MIs using HDAC, granitic porphyry wafers hosting MIs were cut from the same granitic porphyry samples used for heating experiments in the Linkam stage by Wang (2014) and then double-polished. Large, isolated, regularly-shaped MIs were selected for HDAC homogenization experiments (HDAC-VT, Li et al. 2016). The HDAC-VT sample chamber consists of a hole (diameter 1.0 mm) at the center of a Re gasket (diameter 3.0 mm, thickness 0.25 mm) placed between the two diamond-anvil faces (diameter 1.6 mm). Sample temperatures in the sample chamber were measured via two calibrated K-type thermocouples with their temperature sensing tips attached separately to the two diamonds. The

148 thermocouples were calibrated using the triple point of H_2O (0.01 °C) and the melting
149 points of $NaNO_3$ (306.8 °C) and NaCl (800.5 °C). The reported temperatures were
150 precise to ± 0.5 °C and accurate to ±1.5 °C for those above 380 °C.

151 In the experiments, a quartz wafer piece hosting MIs, deionized water, and vapor
152 bubble(s) were sealed in the sample chamber through the compression of the two
153 diamond anvils of the HDAC (Fig. 3). The wafer piece was <1.0 mm in length and
154 width, and ~0.15 mm in thickness, so that the wafer piece would not break while
155 sealing the sample chamber. During heating, the initial heating rate was 5 °C/min up
156 to a temperature of 400 °C. A rate of 1 °C/min was then maintained until total
157 MI-homogenization. Following these heating steps, a MI-homogenization experiment
158 took 6–8 hours. In addition, at temperatures exceeding 200 °C, a continuous flow of a
159 mixed gas (98% Ar and 2% H_2) outside of the HDAC sample chamber was kept to
160 protect the HDAC's diamond anvils and resistance heating wires from oxidation.

161 During heating, the pressure in the HDAC chamber was calculated from the
162 known bulk H_2O density and temperature in the chamber using the equation of state
163 of Wagner and Pruβ (2002). The bulk H_2O density was determined by the temperature
164 (T_{hDC}) at which the vapor bubble disappeared in the HDAC sample chamber. T_{hDC} in
165 each experiment was measured in the heating process and again during reheating after
166 generation of a vapor phase in the cooling process; the latter measurement was used to
167 calculate the H_2O density according to the equation of state of H_2O (Wagner and Pruβ
168 2002). In this paper, we adjusted the T_{hDC} to 370–373 °C in each case, by shrinking

the sample chamber or leaking a certain amount of H_2O from the sample chamber by tightening or loosening the HDAC pressurizing screws as needed. Accordingly, the H_2O loaded in the sample chamber exhibited a density of 451.43–398.68 kg/m^3, and pressures of ~200 MPa were applied at 800 °C to the MIs in the sample chamber. Such pressure roughly balanced with the internal pressure of MIs, since estimated metallogenic pressures of porphyry deposits are about 100–200 MPa (Cline 1995; Richards 2011). Hence, MI volume stretching was minimized, and MI decrepitation was prevented during heating.

Wang (2014) performed MI-homogenization experiments at one atmosphere in a Linkam TS1500 heating stage, referring to the heating process described by Esposito et al. (2012). In the experiments, the heating stage was calibrated using the melting temperature of NaCl (800.5 °C). The difference between the known melting temperature of the calibration standard and the measured temperature was always <5 °C. In Wang's experiments, MIs hosted in quartz wafer (~0.2 mm in thickness) were observed through a ZEISS Axioskop 50× optical microscope. Below 500 °C, a heating rate of 5 °C/min was maintained; after holding at 500 °C for half an hour, MIs continued to be heated at a rate of 1 °C/min until total MI-homogenization.

In the MI-homogenization experiments, the heating rate was critical for obtaining exact temperatures (Danyushevsky et al. 2002). A high heating rate could result in the melting process lagging behind, yielding measured transition temperatures higher than the true values. On the other hand, a low heating rate could

lead to re-equilibration (i.e., equilibration at conditions different from those at the moment of trapping) of a MI with its host, or even diffusion of volatiles such as H_2O (Severs et al. 2007). In the present paper, the heating rate of 1 °C/min ensured thermal equilibrium inside each MI while preventing the diffusion of volatiles during heating, according to kinetic experiments performed by Danyushevsky et al. (2002) and Student and Bodnar (1999).

EXPERIMENTAL RESULTS

Table 1 provides the experimental microthermometry results for the MIs in quartz phenocrysts in granitic porphyry from the Yixingzhai Au deposit using HDAC. In the MI heating process, the solid phases in each MI began to melt as the temperature reached the MI's initial melting temperature (T_{IniM}). During further heating, the MI's remaining solid phase seemingly melted into a molten state at the total melting temperature (T_{TotM}) of the solid phases (Fig. 4), with the possibility that at T_{TotM} few fine-feldspar crystals (not visible) could remain in contact with the vapor bubble or on the MI wall as suggested by Student and Bodnar (2004). This vapor phase coexisted with the melt phase in each MI until the vapor phase totally dissolved into the melt, yielding a total homogenization temperature (T_{hTot}) of the MI. After being totally homogenized, each MI occupied a larger volume than before heating, transformed from an irregular or negative crystal shape to a round or elliptical shape (Fig. 4). This transformation indicated that the crystallized phases on the MI wall were melted, in keeping with the known characteristics of MIs before and after

homogenization in igneous rocks (Frezzotti 2001). Additionally, the heating results of MIs performed using a Linkam stage by Wang (2014) are listed in Table 2, and the phase transition process of one representative MI during heating is shown in Fig. 5.

As shown in Figs. 4 and 5, the phase transition sequence and behavior of MI in homogenization experiments using a Linkam TS1500 stage were qualitatively similar to those obtained using HDAC. However, close comparison reveals the robust effects of elevated external pressure on MIs' measured phase transition temperatures (Tables 1 and 2). T_{IniM}, T_{TotM}, and T_{hTot} as measured using the Linkam stage were 719–826 °C, 845–1046 °C, and 943–1190 °C, respectively (Table 3; Fig. 6). These values were up to 374 °C higher than the corresponding values obtained using HDAC: 675–720 °C, 760–791 °C, and 816–850 °C, respectively (Table 3; Fig. 7).

DISCUSSION

Phase transition temperatures of melt inclusions estimated from homogenization experiments with Linkam stage

As shown in Tables 1, 2, and 3, the MI-homogenization results using HDAC and using the Linkam stage are substantially different. Such differences can be ascribed to the external pressure applied to the MIs during heating, as the external pressure can prevent decrepitation and volatile diffusion or leakage (Thomas and Davidson 2016a). When the MIs were heated at one atmosphere, homogenization was slow due to high melt viscosity and a correspondingly low diffusivity for escaping volatiles (Hurai et al. 2015). Consequently, the measured MI T_{hTot} using the Linkam stage is significantly

greater than the equilibrium temperature at which the aqueous phase is separated from the melt inside MIs during cooling at depth.

Generally, MIs of small size possess little absolute wall area for volatile diffusion during the heating process, as volatiles mainly escape through either preexisting or strain-induced dislocations and decrepitation cracks (Hurai et al. 2015; Severs et al. 2007), as well as along microcracks that form at the quartz α–β transition at ~573 °C at one atmosphere pressure (Severs et al. 2007). Usually, in hours, the diffusion of H_2O to or from MIs can occur during heating (Cannatelli et al. 2016; Chen et al., 2011; Massare et al. 2002; Portnyagin et al. 2007), particularly when the MIs are hosted in a thin mineral wafer rather than relatively large mineral grains in the heating experiments. Hence, at a constant heating rate, MI-homogenization temperatures are controlled by diffusion as a function of inclusion volume and the duration of the heating experiment as described by Thomas (1994). As a consequence, this can be seen as a correlation between inclusion size and phase transition temperature as was found in homogenization experiments using the Linkam stage, even though MIs were heated in several hours (Student and Bodnar 1999). This phenomenon has also been observed in MI-homogenization experiments using a furnace. In these experiments, MIs were heated to a constant temperature higher than the solidus for the given melt composition and then quenched to analyze possible evidence of homogenization (Thomas 1994; Thomas and Klemm 1997). In such quenching homogenization experiments with a constant 20-hour heating duration, the phase transition

253 temperatures of MIs and the corresponding diameters of MIs showed a clear linear
254 relationship (Thomas 1994). This positive correlation was used to infer the true phase
255 transition temperature at a theoretical inclusion size of zero, for which no diffusion
256 kinetics would bias the measurement (Hurai et al. 2015; Student and Bondar 1999).
257 Similarly, we use data measured at one atmosphere in a Linkam stage by Wang (2014)
258 to extrapolate the relationship between T_{htot} and diameter to an infinitesimally-small
259 MI (Fig. 6). These data show a good linear correlation of T_{hTot} (°C) = 11.748 d + 825,
260 where d represents MI diameter in μm, as shown in Fig. 6. Similarly, the correlations
261 of T_{TotM} and T_{IniM} with MI size can roughly be expressed by T_{TotM} (°C) = 9.1928 d +
262 760 and T_{IniM} (°C) = 3.3436 d + 690, respectively. These latter correlations exhibited
263 relatively low correlation coefficients, possibly because T_{TotM} and T_{IniM} were difficult
264 to determine with high precision through observation. These correlations, all positive,
265 indicate that these MIs hosted in quartz from porphyry samples were trapped from
266 uniform magma at a similar temperature, as indicated in experiments by Student and
267 Bodnar (1999). Moreover, the slopes in the linear equations of T_{hTot}, T_{TotM}, and T_{IniM}
268 vs. MI diameter decreased in that sequence (Fig. 6), indicating the effects of MI
269 volatile diffusion on phase transition temperatures during heating. Based on these
270 positive correlations, we extrapolated linearly to determine the T_{hTot}, T_{TotM}, and T_{IniM}
271 of a hypothetical, infinitesimally small MI (diameter = 0 μm). These estimates were
272 ~825 °C, ~760 °C, and ~690 °C, respectively, among which the extrapolated T_{hTot}
273 (825 ± 8 °C) exhibits relatively small error, closely approximating the actual T_{hTot}.

This is the peer-reviewed, final accepted version for American Mineralogist, published by the Mineralogical Society of America.
The published version is subject to change. Cite as Authors (Year) Title. American Mineralogist, in press.
DOI: https://doi.org/10.2138/am-2021-7781. http://www.minsocam.org/

Phase transition temperatures of melt inclusions measured using hydrothermal diamond-anvil cell

Granitic porphyry deposits typically form at pressures of 100–200 MPa (Cline 1995; Richards 2011), so such pressures could be assumed for the studied MIs. After the homogenization of fluid phases during heating, however, the internal pressure would have increased along the fluid isochores, potentially reaching a higher pressure than the MI trapped pressure prior to homogenization (Fig. 8; Student and Bodnar 1996). Therefore, in our homogenization experiments of MIs using HDAC, external pressures of ~(140–230) MPa were exerted on the MIs after initial melting of the solid phase (Table 1). The phase transition temperatures of MIs as measured using HDAC (T_{hTot} = 833 ± 17 °C, T_{TotM} = 780 ± 15 °C, and T_{IniM} = 695 ± 20 °C; Fig. 7a) were identical, within error, to the temperature ranges estimated from the linear correlations of phase transition temperatures measured at one atmosphere with MI size as shown in Fig. 6. Moreover, T_{hTot}, T_{TotM} and T_{IniM} did not show the effects of external pressures and MI size on measured phase transition temperatures (Fig. 7). This finding indicates that no significant diffusion that occurred in MIs heated at one atmosphere using the Linkam stage occurred during heating using HDAC.

The MI-homogenization process showed that the bubble finally dissolved into a hydrous melt phase, indicating that the MIs homogenized into H_2O-saturated melt. Moreover, as shown in Fig. 2b, the coexistence of MIs and FIs indicates that silicate MIs were trapped from H_2O-saturated melt (Student and Bodnar 1999), from which

aqueous fluids exsolved. Therefore, the T_{hTotS} represent the trapping temperatures of MIs. Wang et al. (2010) used the whole-rock zirconium saturation thermometer to estimate the average crystallization temperature of the Dexing granodiorite porphyry rock mass to be 790 ± 50 °C. Student and Bodnar (2004) homogenized the MIs hosted in quartz phenocrysts of quartz latite from Red Mountain, Arizona, USA, under pressure in a cold-seal pressure vessel at 810–835 °C. These temperatures are compatible with the present homogenization temperature results for MIs in the Yixingzhai Au deposit using HDAC.

In summary, the MI-homogenization temperatures measured in HDAC experiments at suitably elevated external pressures could be close to the actual values, and can be used to indicate the *P–V–T–X* properties of MIs. Moreover, the HDAC experiments directly yield concrete values, in comparison with the linear extrapolation method required for experiments performed using the Linkam stage at one atmosphere (e.g., Fig. 6). This distinction is particularly important from a practical perspective because the linear extrapolation method is extremely time-consuming and can be applied only to samples with numerous primary inclusions originating at the same temperature with a uniform chemical composition, phase composition, and water content. Decrepitation cracks and the entrapment of a heterogeneous melt-fluid mixture make the use of this method impossible (Hurai et al. 2015).

Entrapment conditions of melt inclusions inferred from homogenization

316 **experiments using hydrothermal diamond-anvil cell**

317 Based on the phase changes in granitic melt inclusions suggested by Student and
318 Bodnar (1996) and Hurai et al. (2015), the *P*–*T* trajectory of the MIs during heating is
319 described in Fig. 8. With increasing temperature, the fluid phases inside MI
320 homogenize into liquid or vapor (point A in Fig. 8), although such a process was not
321 clearly observed in the studied MIs. Subsequently, the *P*–*T* trajectory of the MI moves
322 along the fluid isochore, and the incipient melting of solid phases occurs when the
323 isochore intersects the fluid-saturated solidus of the granitic magma at the MI's T_{IniM}
324 (point B in Fig. 8). With the onset of melting, the fluid phase volume decreases as the
325 fluid phase gradually dissolves in the melt (range C between points B and D in Fig. 8)
326 until total melting of solid phases at the MI's T_{TotM}. Finally, fluid is totally dissolved
327 into the melt phase at point D in Fig. 8, corresponding to T_{hTot} on the H_2O-saturated
328 liquidus. The T_{hTot} and the corresponding MI homogenization pressure represent the
329 MI trapping *P*–*T* conditions as MIs were trapped from H_2O-saturated granitic melt.

330 As shown in Fig. 8, the MI trapping pressure can be roughly determined by the
331 intersection of the isochore of the fluid phase within the MI and the water-saturated
332 solidus curve for granite, as suggested by Audétat and Pettke (2003), Audétat et al.
333 (2008), and Yang and Bodnar (1994). Accordingly, we roughly estimated the trapping
334 pressure of MIs in the Yixingzhai granitic porphyry to be ~140 MPa, based on the
335 H_2O-saturated granite melt solidus and the ~695 °C T_{IniM} of MIs (Fig. 8). This figure
336 agrees with the reported 100–200 MPa estimates of the metallogenic pressure of

337 granitic porphyry-type Cu–Au deposits (Cline 1995; Richards 2011). Moreover, MI
338 H_2O content can be estimated to be ~2 wt% based on the estimated MI trapping
339 pressure (~140 Ma) and T_{hTot} (~836 °C) (Fig. 8), since T_{hTot} corresponds to the
340 liquidus of the H_2O-saturated granite melt at the MI trapping pressure (Li et al. 2017;
341 Poutiainen and Scherbakova 1998). Such H_2O content should be considered as the
342 minimum value, because the presence of additional volatiles (e.g., F, CO_2) would also
343 affect the liquidus temperature (King and Holloway 2002; Manning 1981). Moreover,
344 the 2 wt% H_2O content of MIs is consistent with that (1.6–3.6 wt%) of comenditic
345 pumice and pyroclastic flow as obtained by Li et al (2006), as well as with the 2.1–2.8
346 wt% H_2O contents in granitic magma that produced the skarn-porphyry Cu–Fe–Au
347 deposit in Tieshan, China (Zhou et al. 2020).

348 **IMPLICATIONS**

349 Our study showed that MI-homogenization experiments using heating stages
350 (e.g., the Linkam series stages) at one atmosphere generally yield MI phase transition
351 temperatures significantly higher than the actual occurring temperatures during the
352 melt natural cooling process due to volatile diffusion or leakage from MIs during
353 heating. Therefore, temperatures measured at one atmosphere require detailed
354 interpretation such as the linear extrapolation method described above to account for
355 volatile diffusion before they can be used to research the *P–V–T–X* properties of MIs.
356 However, the extrapolation method is extremely time-consuming and is available only
357 for assemblages of MIs trapped from a uniform magma at a single temperature.

In our study, HDAC was used to exert an appropriate external pressure on MIs to balance the internal pressure of the MI during heating, effectively preventing volatile-rich MI decrepitation and volatile diffusion while allowing the homogenization process to be monitored continuously *in situ*. As a result, in MI-homogenization experiments using HDAC, measured MI phase transition temperatures were not artificially elevated but rather coincided with naturally occurred phase transition temperatures during cooling process, with measured phase transition temperature not affected by MI size. As a result, the measured temperatures were suitable for direct use in calculating the *P–V–T–X* properties of magma such as the H_2O content in granitic magma. Moreover, the new type of HDAC used (HDAC-VT type) was more stable than previous versions, and was able to run under high *P–T* conditions for a long time under the control of a computer, so that HDAC is no longer laborious for MI-homogenization. Moreover, a cooling system was designed for HDAC (Li et al. 2020), which benefits for the fast quenching of MIs samples in homogenization experiments. Therefore, we recommend the further adoption of the HDAC as a tool for MI-homogenization experiments based on the advantages demonstrated in this study.

ACKNOWLEDGMENTS

We thank Dr. Rainer Thomas and one anonymous reviewer for their constructive reviews. This study was supported by National Key R&D program of China (2019YFC0605200), Shandong Provincial Natural Science Foundation

(ZR2020QD029), Study on Chronological Determination and Testing Methods of Important Magmatic Rocks in Shandong Province (Lukanzi (2019) 8), Study on Metallogenesis of Typical Metallogenic Areas of Gold, Rare Metal and Rare Earth Element Minerals in Shandong Province (Lukanzi (2020) 7), Shandong Provincial Natural Science Foundation (ZR2019PD019) and the Key Frontier Science Program (QYZDY-SSW-DQC008) of Chinese Academy of Sciences.

REFERENCES CITED

Anderson, A.T., Davis, A.M., and Lu, F. (2000) Evolution of Bishop tuff rhyolitic magma based on melt and magnetite inclusions and zoned phenocrysts. Journal of Petrology, 41, 449–473.

Audétat, A., and Lowenstern, J.B. (2014) Melt inclusions. In: H.D. Turekian and K.K. Holland, Eds., Treatise on Geochemistry, 2nd ed., p. 143–173. Elsevier, Oxford.

Audétat, A., and Pettke, T. (2003) The magmatic-hydrothermal evolution of two barren granites: a melt and fluid inclusion study of the Rito del Medio and Cañada Pinabete plutons in northern New Mexico (USA). Geochimica et Cosmochimica Acta, 67, 97–121.

Audétat, A., Pettke, T., Heinrich, C.A., and Bodnar, R.J. (2008) The composition of magmatic-hydrothermal fluids in barren and mineralized intrusions. Economic Geology, 103, 877–908.

Bartoli, O., Cesare, B., Poli, S., Bodnar, R.J., Frezzotti, M.L., Acosta-Vigil, A., and Meli, S. (2011) Melting in the deep crust: message from melt inclusions in

400 peritectic garnet from migmatites. Mineralogical Magazine, 75, 495.

401 Bassett, W.A., Shen, A.H., Bucknum, M., and Chou, I-M. (1993) A new diamond
402 anvil cell for hydrothermal studies to 2.5 GPa and from -190 to 1200 °C. Review
403 of Scientific Instruments, 64, 2340–2345.

404 Bodnar, R.J., and Student, J.J. (2006) Melt inclusions in plutonic rocks: Petrography
405 and microthermometry. In J.D. Webster, Ed., Melt Inclusions in Plutonic Rocks,
406 p. 1–25. Mineralogical Association of Canada, Short Course, 36.

407 Cannatelli, C., Doherty, A.L., Esposito, R., Lima, A., De Vivo, B. (2016)
408 Understanding a volcano through a droplet: A melt inclusion approach. Journal
409 of Geochemical Exploration, 171, 4–19.

410 Cesare, B., Acosta-Vigil, A., Ferrero, S., and Bartoli, O. (2011) Melt inclusions in
411 migmatites and granulites. In M.A. Forster and J.D. Fitz Gerald, Eds., The
412 Science of Microstructure — Part II. Journal of the Virtual Explorer, 38,
413 doi:10.3809/jvirtex.2011.00268 (Electronic Edition).

414 Chen, Y., Provost, A., Schiano, P., and Cluzel, N. (2011) The rate of water loss from
415 olivine-hosted melt inclusions. Contributions to Mineralogy and Petrology, 162,
416 625–636.

417 Cline, J.S. (1995) Genesis of porphyry copper deposits: the behavior of water,
418 chloride, and copper in crystallizing melts. In F.W. Pierce and J.G. Bolm, Eds.,
419 Porphyry Copper Deposits of the American Cordillera, p. 69–82, Arizona
420 Geological Society Digest 20, Tucson, Arizona.

421 Danyushevsky, L.V., Mcneill, A.W., and Sobolev, A.V. (2002) Experimental and
422 petrological studies of melt inclusions in phenocrysts from mantle-derived
423 magmas: an overview of techniques, advantages and complications. Chemical
424 Geology, 183, 5–24.
425 Esposito, R., Klebesz, R., Bartoli, O., Klyukin, Y.I., Moncada, D., Doherty, A.L., and
426 Bodnar, R.J. (2012) Application of the Linkam TS1400XY heating stage to melt
427 inclusion studies. Central European Journal of Geosciences, 4, 208–218.
428 Fedele, L., Bodnar, R.J., Devivo, B., and Tracy, R.J. (2003) Melt inclusion
429 geochemistry and computer modeling of trachyte petrogenesis at Ponza, Italy.
430 Chemical Geology, 194, 81–104.
431 Ferrero, S., Bartoli, O., Cesare, B., Salviolimariani, E., Acostavigil, A., Cavallo, A.,
432 and Battiston, S. (2012) Microstructures of melt inclusions in anatectic
433 metasedimentary rocks. Journal of Metamorphic Geology, 30, 303–322.
434 Frezzotti, M.L. (2001) Silicate-melt inclusions in magmatic rocks: applications to
435 petrology. Lithos, 55, 273–299.
436 Halter, W.E., Pettke, T., and Heinrich, C.A. (2004) Laser-ablation ICP-MS analysis of
437 silicate and sulfide melt inclusions in an andesitic complex I: analytical approach
438 and data evaluation. Contributions to Mineralogy and Petrology, 147, 385–396.
439 Holtz, F., Johannes, W., Tamic, N., and Behrens, H. (2001) Maximum and minimum
440 water contents of granitic melts generated in the crust: a reevaluation and
441 implications. Lithos, 56, 1–14.

Hurai, V., Huraiova, M., Slobodnik, M., and Thomas, R. (2015) Geofluids: Developments in Microthermometry, Spectroscopy, Thermodynamics and Stable Isotopes, 489 p. Elsevier, Amsterdam.

King, P.L., and Holloway, J.R. (2002) CO_2 solubility and speciation in intermediate (andesitic) melts: the role of H_2O and composition. Geochimica et Cosmochimica Acta, 66, 1627–1640.

Li, J., and Chou, I-M. (2017) Homogenization experiments of crystal-rich inclusions in spodumene from Jiajika lithium deposit, china, under elevated external pressures in a hydrothermal diamond-anvil cell. Geofluids, 2017, 1–12.

Li, J., and Li, S. (2014) Application of hydrothermal diamond anvil cell to homogenization experiments of silicate melt inclusions. Acta Geologica Sinica (English Edition), 88, 854–864.

Li, J., Bassett, W.A., Chou, I-M., Ding, X., Li, S., and Wang, X. (2016) An improved hydrothermal diamond anvil cell. Review of Scientific Instruments, 87, 053108.

Li, J., Chou, I-M., Bassett, W.A., and Wang, X. (2020) A new type of hydrothermal diamond-anvil cell with cooling system. Review of Scientific Instruments, 91, 053104.

Li, N., Metrich, N., and Fan, Q. (2006) FTIR study on water content of the melt inclusions in phenocrysts from Changbaishan Tianchi volcano's great eruption in Holocene. Acta Petrologica Sinica, 22, 1465–1472 (in Chinese with English abstract).

463 Li, S., Li, J., Chou, I-M., Jiang, L., and Ding, X. (2017) The formation of the Yichun
464 Ta-Nb deposit, South China, through fractional crystallization of magma
465 indicated by fluid and silicate melt inclusions. Journal of Asian Earth Sciences,
466 137, 180–193.
467 Lowenstern, J.B. (1994) Dissolved volatile contents in an ore-forming magma.
468 Geology, 22, 893–896.
469 Lowenstern, J.B. (1995) Applications of silicate-melt inclusions to the study of
470 magmatic volatiles. In J.F.H. Thompson, Ed., Magmas, Fluids and Ore Deposits,
471 p. 71–99. Mineralogical Association of Canada, Short Course, 23.
472 Magakyan, R., Sobolev, A.V., Zakariadze, G.S., and Kononkova, N.N. (1993)
473 Petrology of evolved boninite magmas: evidence from the Mesozoic lesser
474 Caucasus island arc. Petrology, 1, 378–394.
475 Manning, D.A.C. (1981) The effective of fluorine on liquidus phase relationships in
476 the system Qz-Ab-Or with excess water at 1 kb. Contributions to Mineralogy and
477 Petrology, 76, 206–215.
478 Massare, D., Metrich, N., and Clocchaitti, R. (2002) High-temperature experiments on
479 silicate melt inclusions in olivine at 1 atm: inference on temperatures of
480 homnogenization and H_2O concentrations. Chemical Geology, 183, 87–98.
481 Portnyagin, M., Hoernle, K., Plechov, P., Mironov, N., and Khubunaya, S. (2007)
482 Constraints on mantle melting and composition and nature of slab components in
483 volcanic arcs from volatiles (H_2O, S, Cl, F) and trace elements in melt inclusions

484 from the Kamchatka Arc. Earth and Planetary Science Letters, 255, 53–69.

485 Poutiainen, M., and Scherbakova, T.F. (1998) Fluid and melt inclusion evidence for
486 the origin of idiomorphic quartz crystals in topaz-bearing granite from the Salmi
487 batholith, Karelia, Russia. Lithos, 44, 141–151.

488 Qin, Z., Lu, F. and Anderson, A.T. (1992): Diffusive reequilibration of melt and fluid
489 inclusions. American Mineralogist, 77, 565–576.

490 Raia, F., Webster, J.D., and Devivo, B. (2000) Pre-eruptive volatile contents of
491 Vesuvius magmas: constraints on eruptive history and behavior. I. — The
492 medieval and modern interplinian activities. European Journal of Mineralogy, 12,
493 179–193.

494 Reyf, F.G. (1997) Direct evolution of W-rich brines from crystallizing melt within the
495 Mariktikan granite pluton, west Transbaikalia. Mineralium Deposita, 32, 475–490.

496 Richards, J.P. (2011) Magmatic to hydrothermal metal fluxes in convergent and
497 collided margins. Ore Geology Reviews, 40, 1–26.

498 Roedder, E. (1979) Origin and significance of magmatic inclusions. Bulletin De
499 Mineralogie, 102, 487–510.

500 Schiano, P. (2003) Primitive mantle magmas recorded as silicate melt inclusions in
501 igneous minerals. Earth-Science Reviews, 63, 121–144.

502 Severs, M.J., Azbej, T., Thomas, J.B., Mandeville, C.W., and Bodnar, R.J. (2007)
503 Experimental determination of H_2O loss from melt inclusions during laboratory
504 heating: Evidence from Raman spectroscopy. Chemical geology, 237, 358–371.

505 Skirius, C., Peterson, J.W., and Anderson, A.T. (1990) Homogenizing rhyolitic glass
506 inclusions from the Bishop Tuff. American Mineralogist, 75, 1381–1398.
507 Smirnov, S.Z., Peretyazhko, I.S., Zagorsky, V.E., and Mikhailov, M.Y. (2003)
508 Inclusions of unusual late magmatic melts in quartz from the Oktyabr'skaya
509 pegmatite vein, Malkhan field (Central Transbaikal Region). Doklady Earth
510 Sciences, 392, 999–1003.
511 Stockstill, K.R., McSween, H.Y., and Bodnar, R.J. (2005) Melt inclusions in augite of
512 the Nakhla Martian meteorite: Evidence for basaltic parental melt. Meteoritics
513 and Planetary Science Archives, 40, 377–395.
514 Student, J.J., and Bodnar, R.J. (1996) Melt inclusion microthermometry: petrologic
515 constraints from the H_2O-saturated haplogranite system. Petrology, 4, 291–306.
516 Student, J.J., and Bodnar, R.J. (1999) Synthetic fluid inclusions XIV: coexisting
517 silicate melt and aqueous fluid inclusions in the haplogranite-H_2O-NaCl-KCl
518 system. Journal of Petrology, 40, 1509–1525.
519 Student, J.J., and Bodnar, R.J. (2004) Silicate melt inclusions in porphyry copper
520 deposits: Identification and homogenization behavior. Canadian Mineralogist, 42,
521 1583–1599.
522 Thomas, J.B., Bodnar, R.J., Shimizu, N., and Chesner, C.A. (2003) Melt Inclusions in
523 Zircon. Reviews in Mineralogy and Geochemistry, 53, 63–87.
524 Thomas, R. (1994) Estimation of the viscosity and the water content of silicate melts
525 from melt inclusion data. European Journal of Mineralogy, 6, 511–535.

526 Thomas, R. (2000) Determination of water contents of granite melt inclusions by
527 confocal laser Raman microprobe spectroscopy. American Mineralogist, 85,
528 868–872.
529 Thomas, R., and Davidson, P. (2016a) Revisiting complete miscibility between
530 silicate melts and hydrous fluids, and the extreme enrichment of some elements
531 in the supercritical state - consequences for the formation of pegmatites and ore
532 deposits. Ore Geology Reviews, 72 1088–1101.
533 Thomas, R., and Davidson, P. (2016b) Origin of miarolitic pegmatites in the
534 Königshain granite/Lusatia. Lithos, 260, 225–241.
535 Thomas, R., and Klemm, W. (1997) Microthermometric study of silicate melt
536 inclusions in Variscan granites from SE Germany: volatile contents and
537 entrapment conditions. Journal of Petrology, 38, 1753–1765.
538 Thomas, R., and Webster, J.D. (2000) Strong tin enrichment in a pegmatite-forming
539 melt. Mineralium Deposita, 35, 570–582.
540 Thomas, R., Webster, J.D., Rhede, D., Siefert, W., Ricker, K., Forster, H., and
541 Davidson, P. (2006) The transition from peraluminous to peralkaline granitic
542 melts: Evidence from melt inclusions and accessory minerals. Lithos, 91, 137–
543 149.
544 Wagner, W., and Pruss, A. (2002) The IAPWS formulation 1995 for the
545 thermodynamic properties of ordinary water substance for general and scientific
546 use. Journal of Physical and Chemical Reference Data, 31, 387–535.

547 Wang, D., Bi, X., and Shang, L. (2010) The concentration characteristics of HF and
548 HCl deriving from early crystal of granodiorite porphyry in Dexing County
549 Jiangxi Province, China. Acta Mineralogica Sinica, 30, 331–337 (in Chinese with
550 English abstract).
551 Wang, X. (2014) Study on the methods of homogenization experiment of melt
552 inclusions and water content of melt, 57 p. Master thesis, China University of
553 Geosciences, Beijing (in Chinese with English abstract).
554 Webster, J.D., Thomas, R., Rhede, D., Förster, H-J., and Seltmann, R. (1997) Melt
555 inclusions in quartz from an evolved peraluminous pegmatite: Geochemical
556 evidence for strong tin enrichment in fluorine-rich and phosphorus-rich residual
557 liquids. Geochimica et Cosmochimica Acta, 61, 2589–2604.
558 Webster, J.D., and Thomas, R. (2006) Silicate melt inclusion in felsic plutons: a
559 synthesis and review. In J.D. Webster, Ed., Melt Inclusions in Plutonic Rocks,
560 165–188. Mineralogical Association of Canada, Short Course, 36.
561 Yang, K., and Bodnar, R.J. (1994) Magmatic-hydrothermal evolution in the bottoms
562 of porphyry copper systems: Evidence from the silicate melt and aqueous fluid
563 inclusions in the Gyeongsang Basin, South Korea. International Geology
564 Reviews, 36, 608– 628.
565 Zhou, J., Wang, W., Wyman, D.A., and Zhao, Z. (2020) Petrologic reconstruction of
566 the Tieshan magma plumbing system: Implications for the genesis of
567 magmatic-hydrothermal ore deposits within originally water-poor magmatic

568 systems. Journal of Petrology, 61, egaa056,
569 https://doi.org/10.1093/petrology/egaa056.
570

571 **FIGURE CAPTIONS**

572 Figure 1. Petrography of quartz porphyry in the Yixingzhai Au deposit, Shanxi
573 Province, China. Quartz porphyry sample was shown in (a) with a marker of quartz
574 (Qtz) phenocryst. Microscopic photos in the cross-polarized light of quartz porphyry
575 are shown in (b, c, and d) in which quartz (Qtz) phenocryst, groundmass (Gm, mainly
576 composing of microcrystalline quartz and feldspar), and melt inclusions (MIs) are
577 marked.

578

579 Figure 2. Photographs of fluid inclusions (FIs), melt inclusions (MIs), and a MI
580 assemblage (MIA) in quartz phenocrysts from the granitic porphyry in the Yixingzhai
581 Au deposit, China.

582

583 Figure 3. Photograph of the hydrothermal diamond-anvil cell sample chamber
584 containing a quartz wafer, deionized water, and vapor bubbles at 25 °C.

585

586 Figure 4. Images showing the homogenization process of one melt inclusion (No. 11
587 in Table 1) in a quartz phenocryst of the quartz porphyry from the Yixingzhai Au
588 deposit using the hydrothermal diamond-anvil cell. The solid phases inside the MI
589 were initially melted at ~682 °C and totally melted at ~783 °C. After the total melting
590 of solid phases, a vapor phase clearly coexisted with the melt until the complete
591 dissolution of the vapor phase into the melt at the total homogenization temperature
592 (835 °C).

593

594 Figure 5. Images showing the homogenization process of one melt inclusion (No. 3 in
595 Table 2) in a quartz phenocryst of the quartz porphyry from the Yixingzhai Au deposit
596 using the Linkam TS1500 stage at one atmosphere of pressure (Wang 2014). The
597 MI-homogenization process here is similar to that observed in the hydrothermal
598 diamond-anvil cell as shown in Fig. 4. The initial and total melting temperatures of
599 solid phases within the MI were at ~780 °C and ~990 °C, respectively, and the vapor
600 phase totally dissolved into the melt at 1144 °C.

601

602 Figure 6. Diagram showing the positive correlations of the initial melting temperature
603 (T_{IniM}; diamonds) and the total melting temperature (T_{TotM}; dots) of the solid phases,
604 and the total homogenization temperature (T_{hTot}; squares) of melt inclusions (MIs)
605 with MI diameter (d) in homogenization experiments performed at one atmosphere
606 using the Linkam TS1500 heating stage.

607

608 Figure 7. Diagram showing the correlations of the initial melting temperature (T_{IniM};
609 diamonds) and the total melting temperature (T_{TotM}; dots) of the solid phases, and the
610 total homogenization temperature (T_{hTot}; squares) of melt inclusions (MIs) with (a)
611 external pressure on MIs and (b) MI diameter in homogenization experiments
612 performed using the hydrothermal diamond-anvil cell.

613

Figure 8. Schematic diagram showing the *P–T* path (bold black line) of melt inclusions (MIs) in homogenization experiments using the hydrothermal diamond-anvil cell. The range of external pressures exerted on MIs during heating is shown as a gray region, determined by the vapor bubble disappearance temperatures (T_{hDCS}) in the HDAC sample chamber. The H_2O-saturated solidus curve and liquidus curves are taken from Holtz et al. (2001). Points A, B, and D correspond to the *P–T* conditions of heating states a, b, and d shown in the inset. Range C between points B and D indicates the possible *P–T* path in the solid phase-melting process during heating. Given the ~695 °C initial melt temperature of MIs and the fluid-saturated granitic magma solidus, the entrapment pressure of the MIs was estimated to be ~140 MPa, and the H_2O content in MIs was estimated to be ~2 wt% according to the H_2O-saturared magma liquidus under the entrapment *P–T* conditions (~140 MPa, ~833 ^{o}C) of the MIs.

628 **TABLE 1.** Microthermometry experimental results for melt inclusions (MIs) in quartz
629 phenocrysts from the Yixingzhai Au deposit, China, using the hydrothermal
630 diamond-anvil cell (HDAC-VT) heating stage.

Exp. Nos.	Size (μm)	T_{hDC} (℃)	P_{IniM} (MPa)	T_{IniM} (℃)	P_{TotM} (MPa)	T_{TotM} (℃)	P_{hTot} (MPa)	T_{hTot} (℃)
1	8	372	160.48	710	184.97	770	203.52	816
2	10	372	164.58	720	192.65	789	217.11	850
3	12	373	139.56	685	175.03	780	200.32	849
4	15	373	150.84	715	178.72	790	199.95	848
5	21	370	166.95	690	212.42	790	235.66	842
6	22	371	166.87	705	199.39	780	222.05	833
7	25	371	162.50	695	203.69	790	227.99	847
8	28	373	150.84	715	179.09	791	199.59	847
9	33	370	166.95	690	201.14	765	230.77	831
10	45	370	162.36	680	198.88	760	227.20	823
11	30	370	163.28	682	209.27	783	232.55	835
12	15	371	153.72	675	199.39	780	216.52	820
13	35	371	155.04	678	198.53	778	220.78	830

631 T_{hDC}—vapor bubble disappearance temperature in the HDAC sample chamber;
632 T_{IniM}—MI's solid phase initial melting temperature; T_{TotM}—MI's solid phase total
633 melting temperature; T_{hTot}—total homogenization temperature of MI; P_{IniM}, P_{TotM}, and
634 P_{hTot}—corresponding pressures in the HDAC-VT sample chamber at points T_{IniM},
635 T_{TotM}, and T_{hTot}, respectively, calculated by employing the equation of state of H_2O
636 provides by Wagner and Pruβ (2002).
637

638 **TABLE 2.** Microthermometry experimental results of melt inclusions (MIs) in quartz
639 phenocrysts from the Yixingzhai Au deposit, China, using the Linkam TS1500 heating
640 stage (Wang 2014).

Exp. Nos.	Size (μm)	T_{IniM} (℃)	T_{TotM} (℃)	T_{hTot} (℃)
1	22	725	950	1079
2	28	750	970	1157
3	26	780	990	1144
4	18	719	928	1043
5	20	730	985	1038
6	31	790	1046	1190
7	26	810	1034	1135
8	10	720	845	943
9	29	826	1042	1162
10	27	816	995	1140

641 Exp. Nos.—experimental numbers; T_{IniM}—MI's solid phase initial melting
642 temperature; T_{TotM}—MI's solid phase total melting temperature; T_{hTot}—total
643 homogenization temperature of MI.
644

645 **TABLE 3.** Ranges of phase transition temperatures from microthermometry
646 experiments on melt inclusions (MIs) from the Yixingzhai Au deposit, China, using
647 the Linkam TS1500 heating stage and the hydrothermal diamond-anvil cell
648 (HDAC-VT).

Heating stage	T_{IniM} (℃)	T_{TotM} (℃)	T_{hTot} (℃)
HDAC-VT	675–720	760–791	816–850
Linkam TS1500	719–826	845–1046	943–1190

649 T_{IniM}—MI's solid phase initial melting temperature; T_{TotM}—MI's solid phase total
650 melting temperature; T_{hTot}—total homogenization temperature of MI.

Fig. 1


a
Qtz
GPMR
cm
2 cm

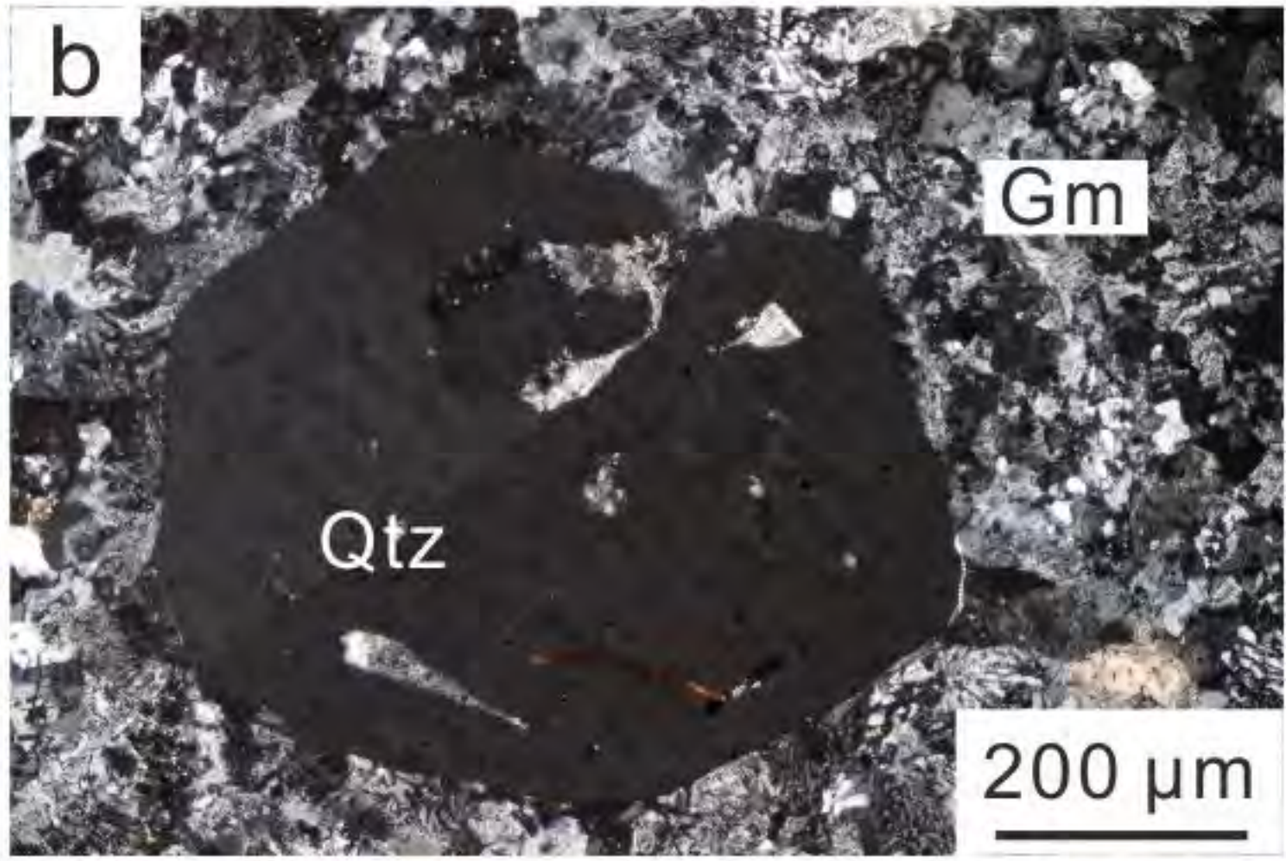
b
Gm
Qtz
200 μm

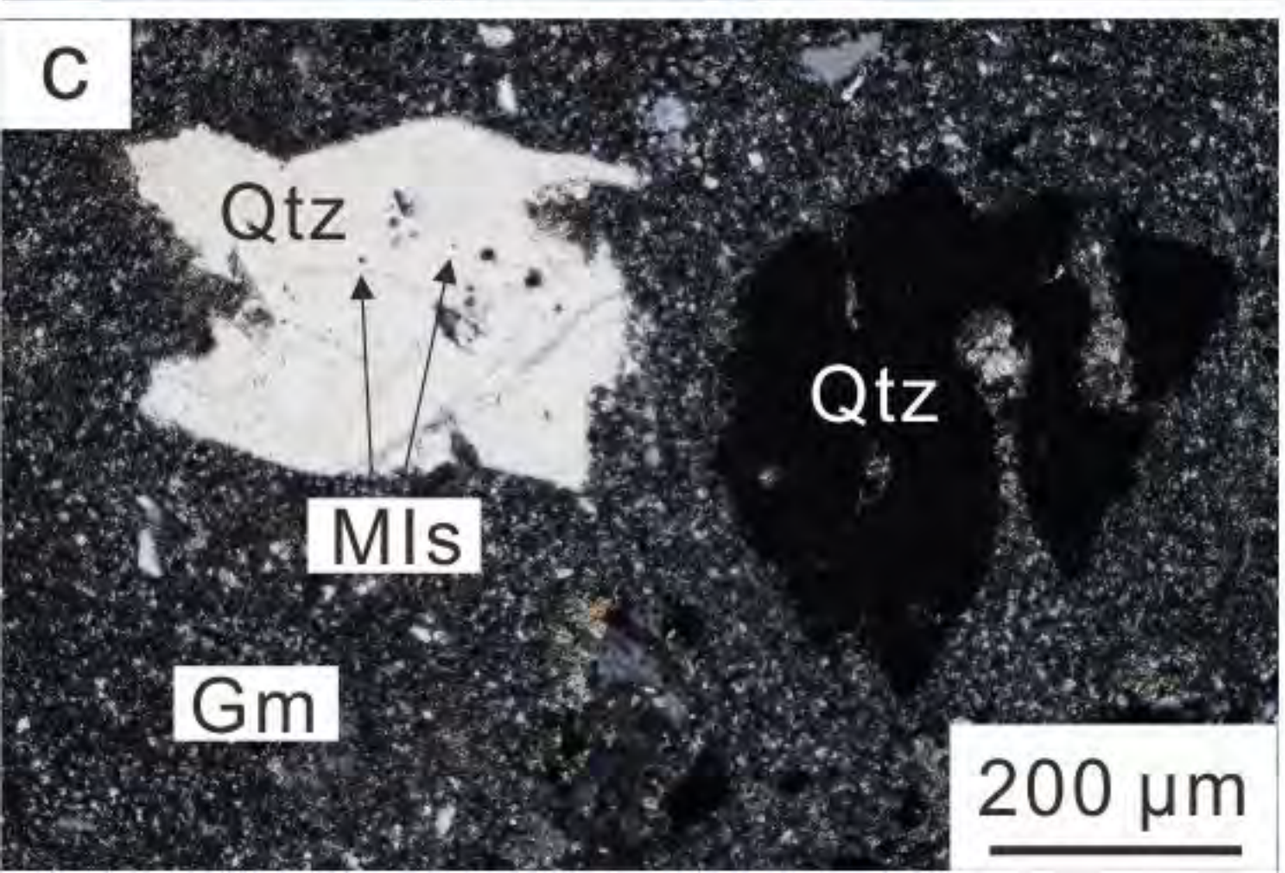
c
Qtz
Qtz
MIs
Gm
200 μm

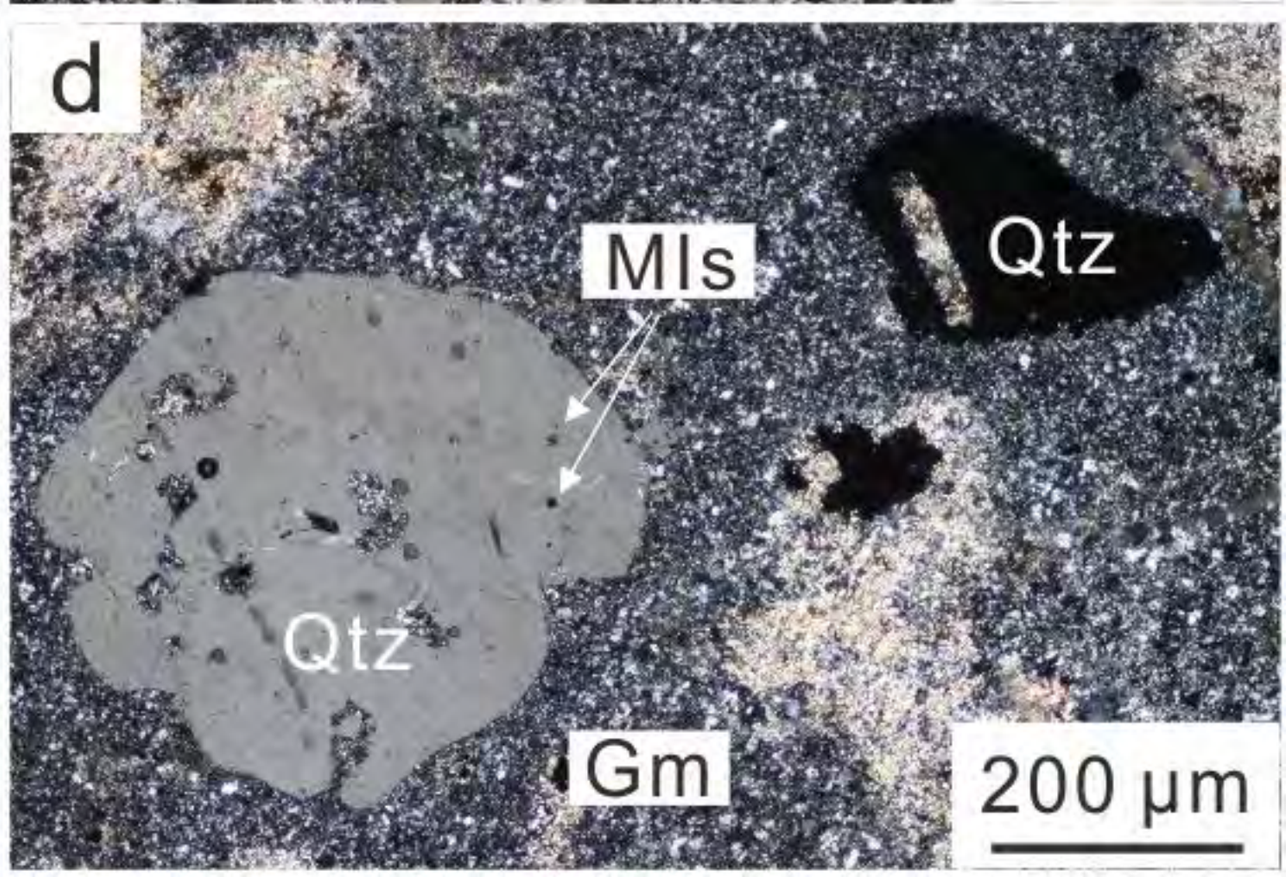
d
MIs
Qtz
Qtz
Gm
200 μm

Fig. 2

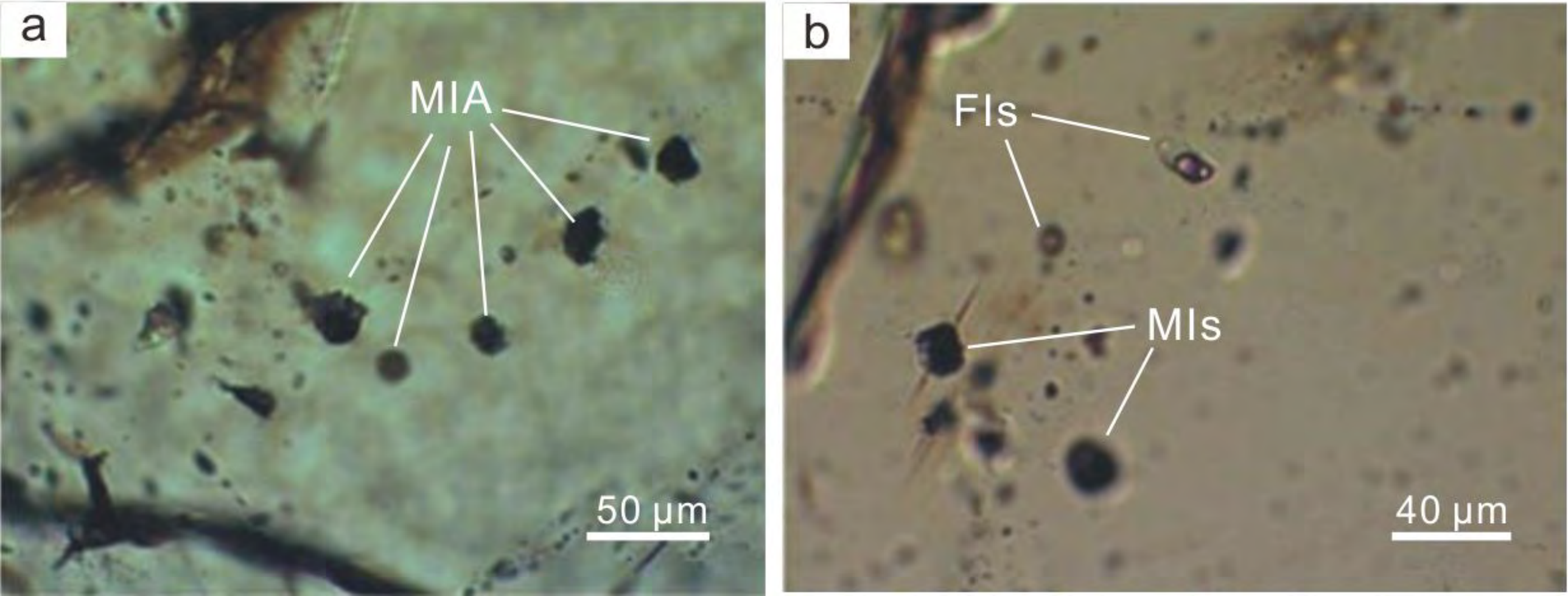

Fig. 3

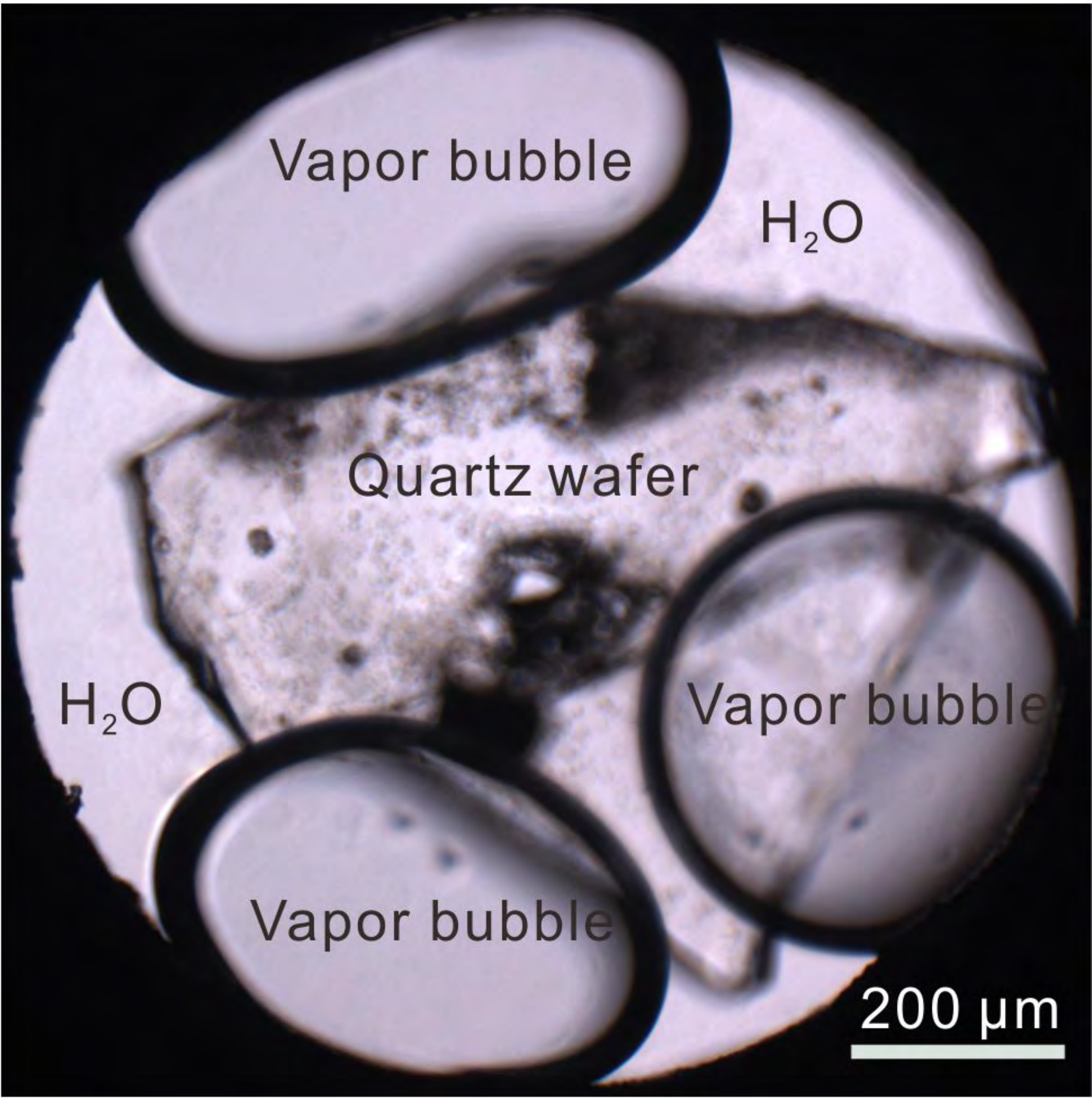
Vapor bubble
H_2O
Quartz wafer
H_2O
Vapor bubble
Vapor bubble
200 µm

Fig. 4

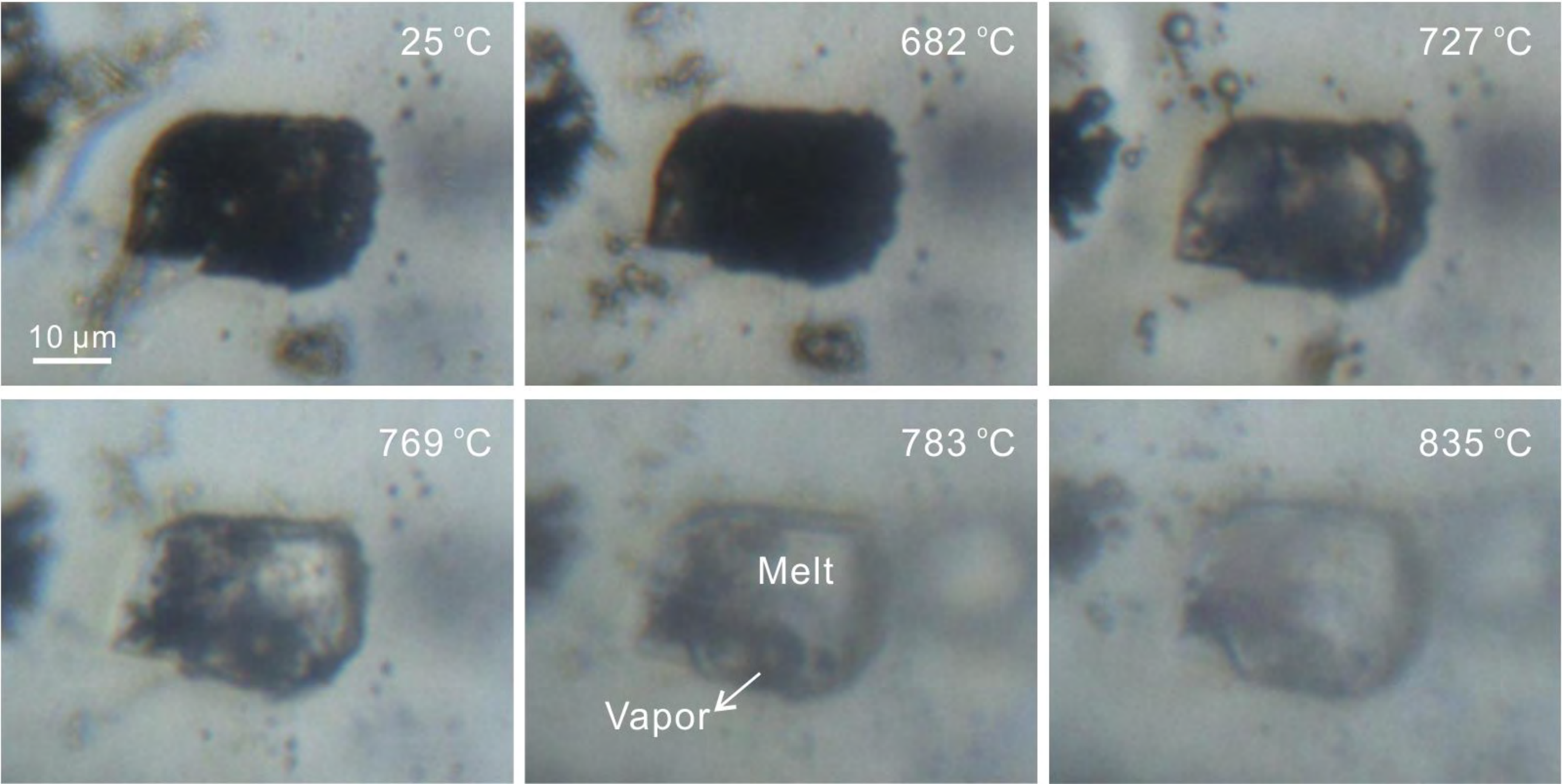

Fig. 5

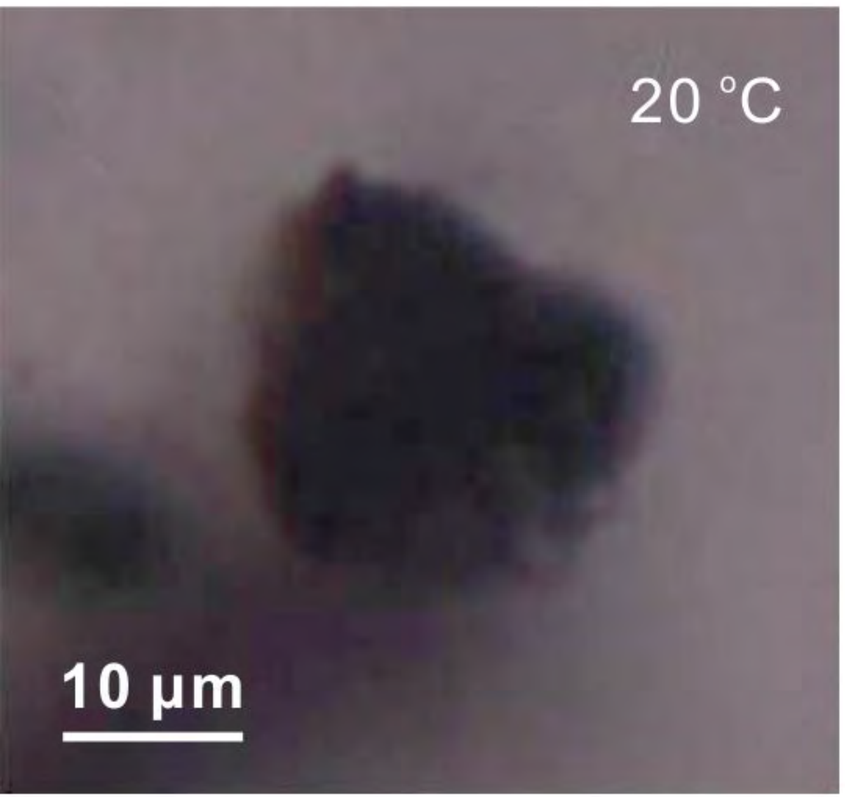
20 °C
10 µm

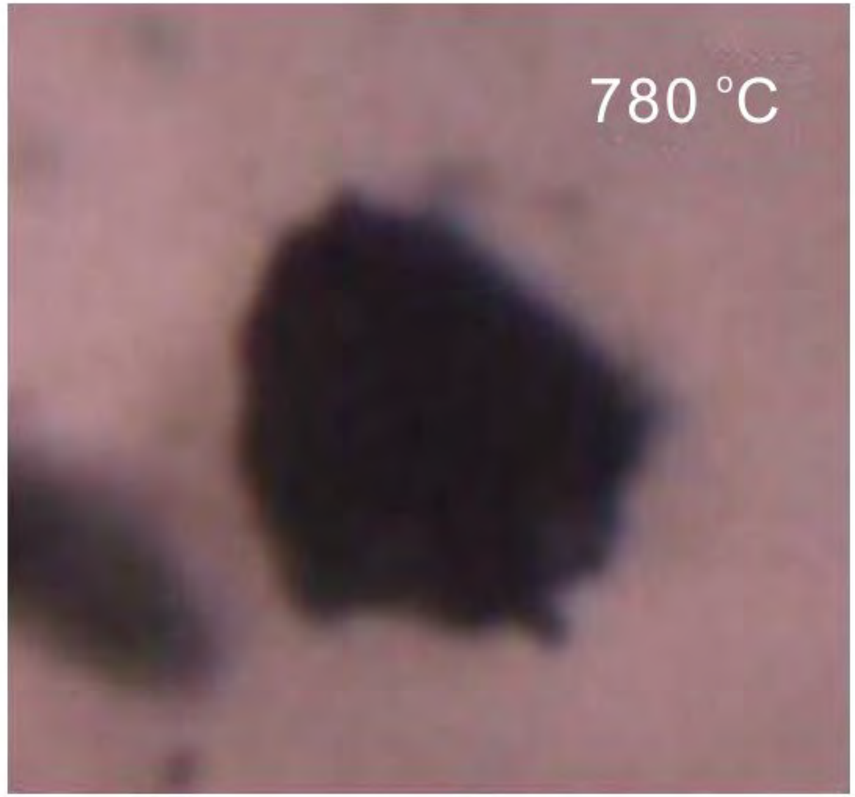
780 °C

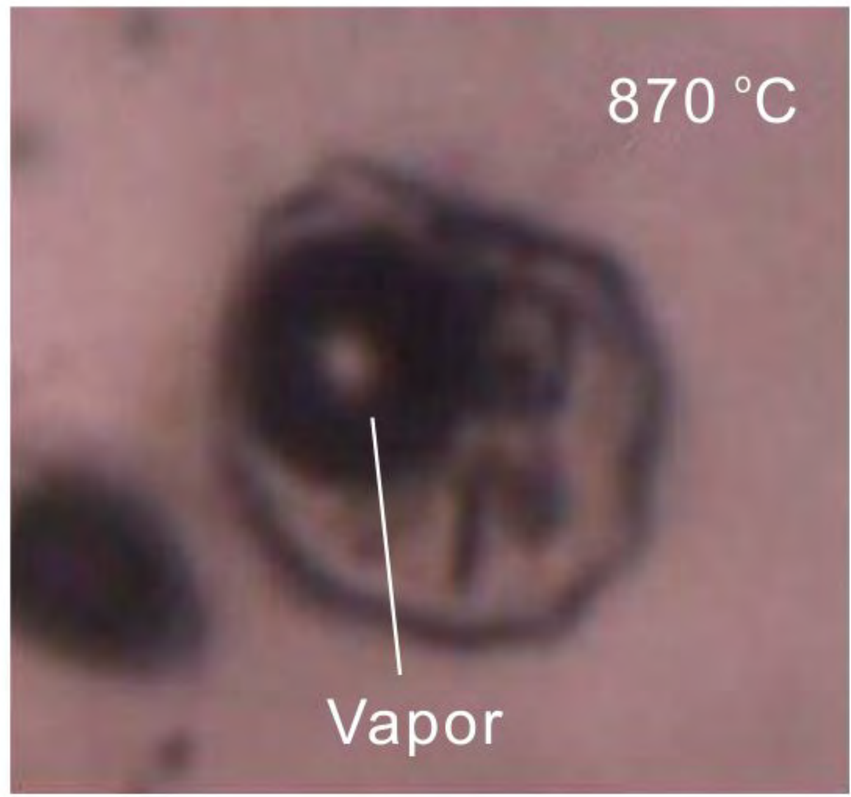
870 °C
Vapor

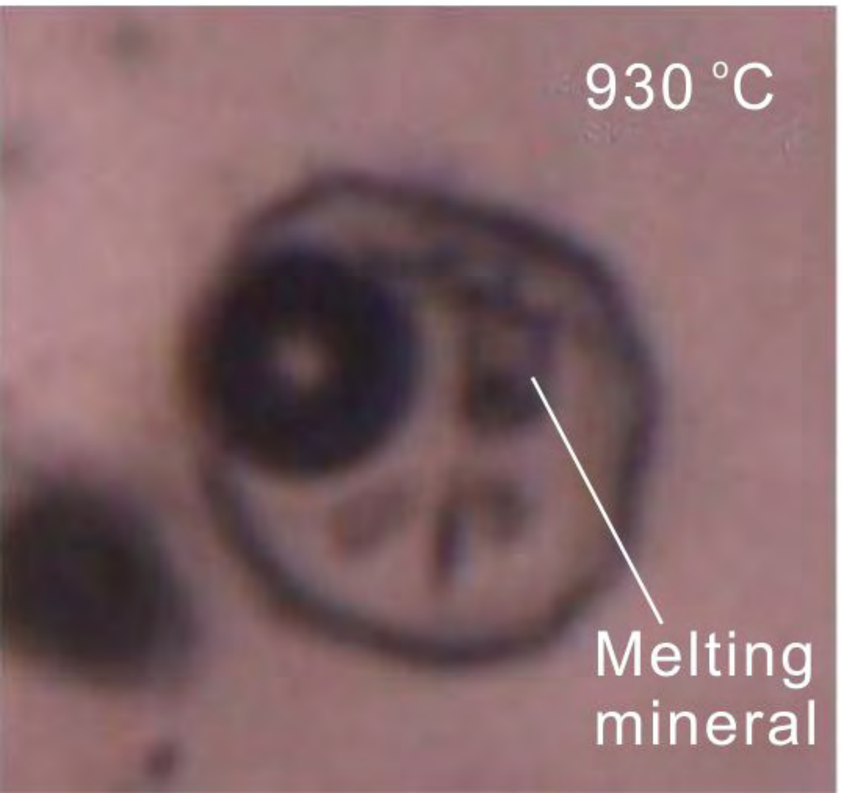
930 °C
Melting
mineral

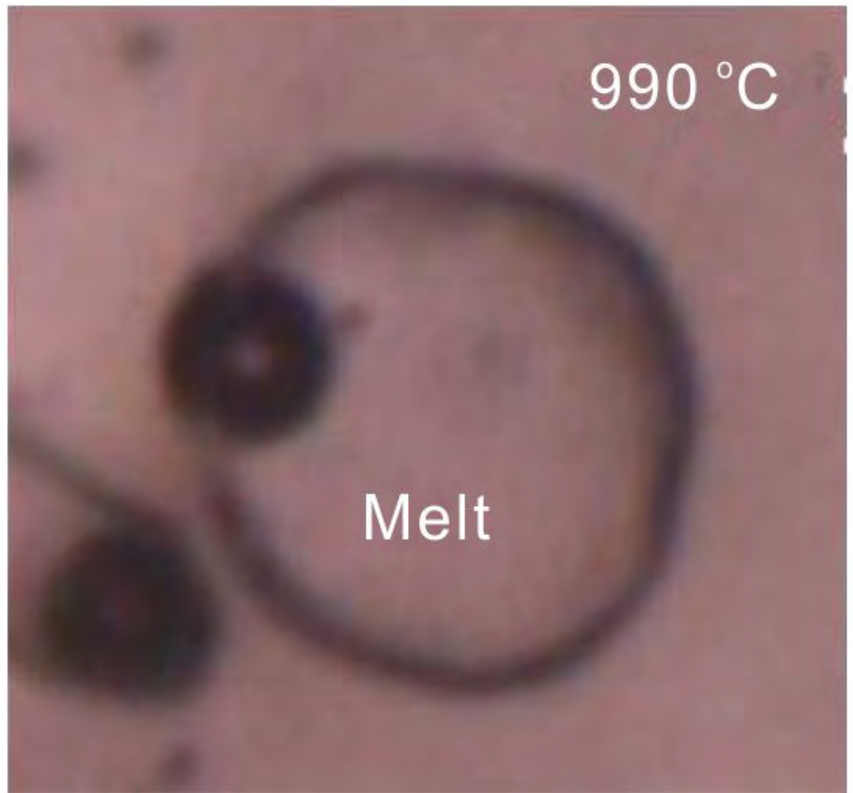
990 °C
Melt

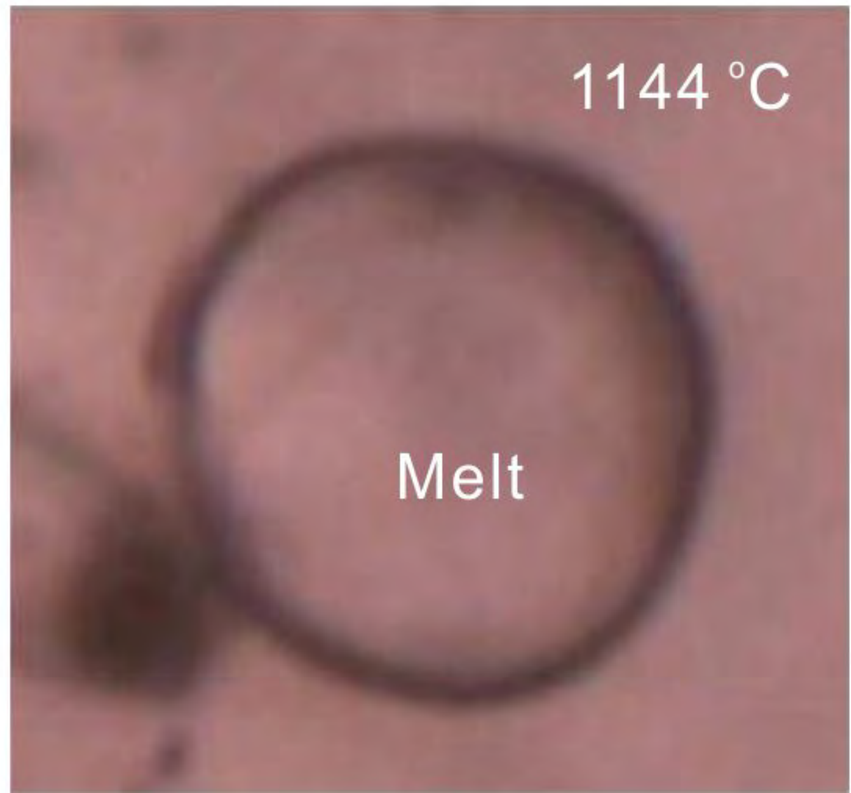
1144 °C
Melt

Fig. 6

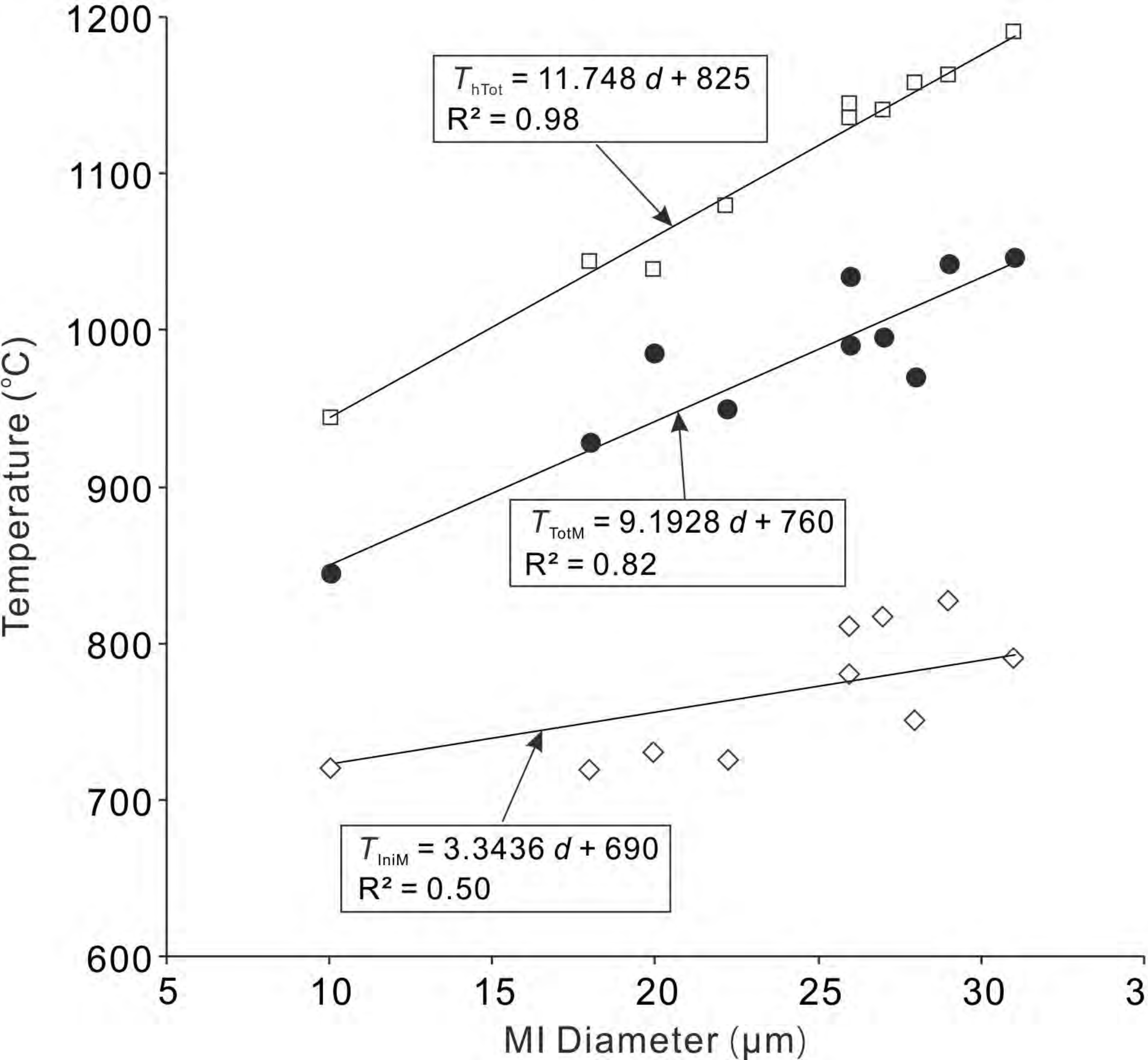
T_{hTot} = 11.748 d + 825
R² = 0.98
T_{TotM} = 9.1928 d + 760
R² = 0.82
T_{IniM} = 3.3436 d + 690
R² = 0.50
Temperature (°C)
MI Diameter (µm)
1200
1100
1000
900
800
700
600
5
10
15
20
25
30
35

Fig. 7

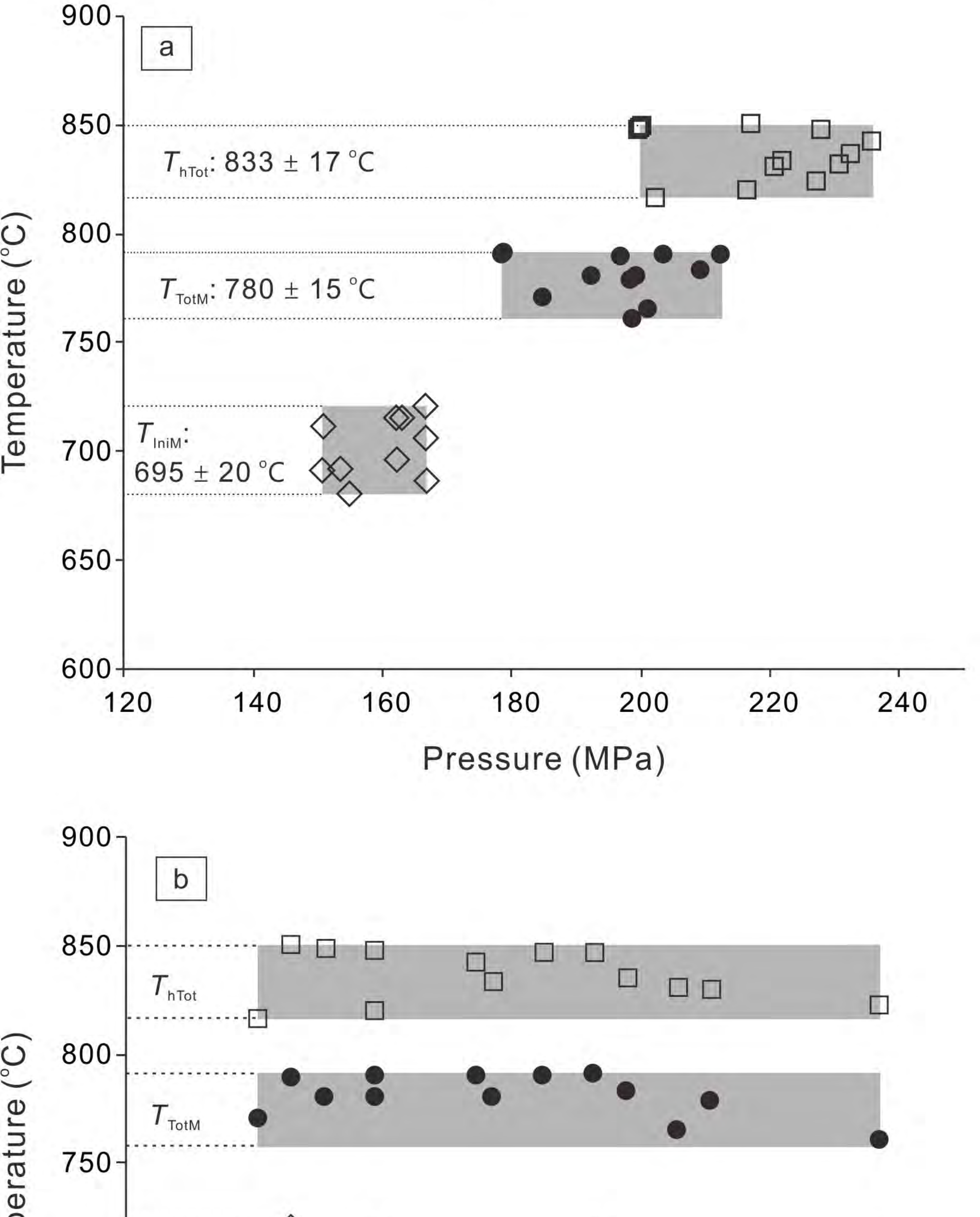
a
900
850
800
750
700
650
600
T_{hTot}: 833 ± 17 °C
T_{TotM}: 780 ± 15 °C
T_{IniM}:
695 ± 20 °C
120
140
160
180
200
220
240
Pressure (MPa)
Temperature (°C)
b
T_{hTot}
T_{TotM}
T_{IniM}
0
10
20
30
40
50
MI Diameter (μm)

Fig. 8

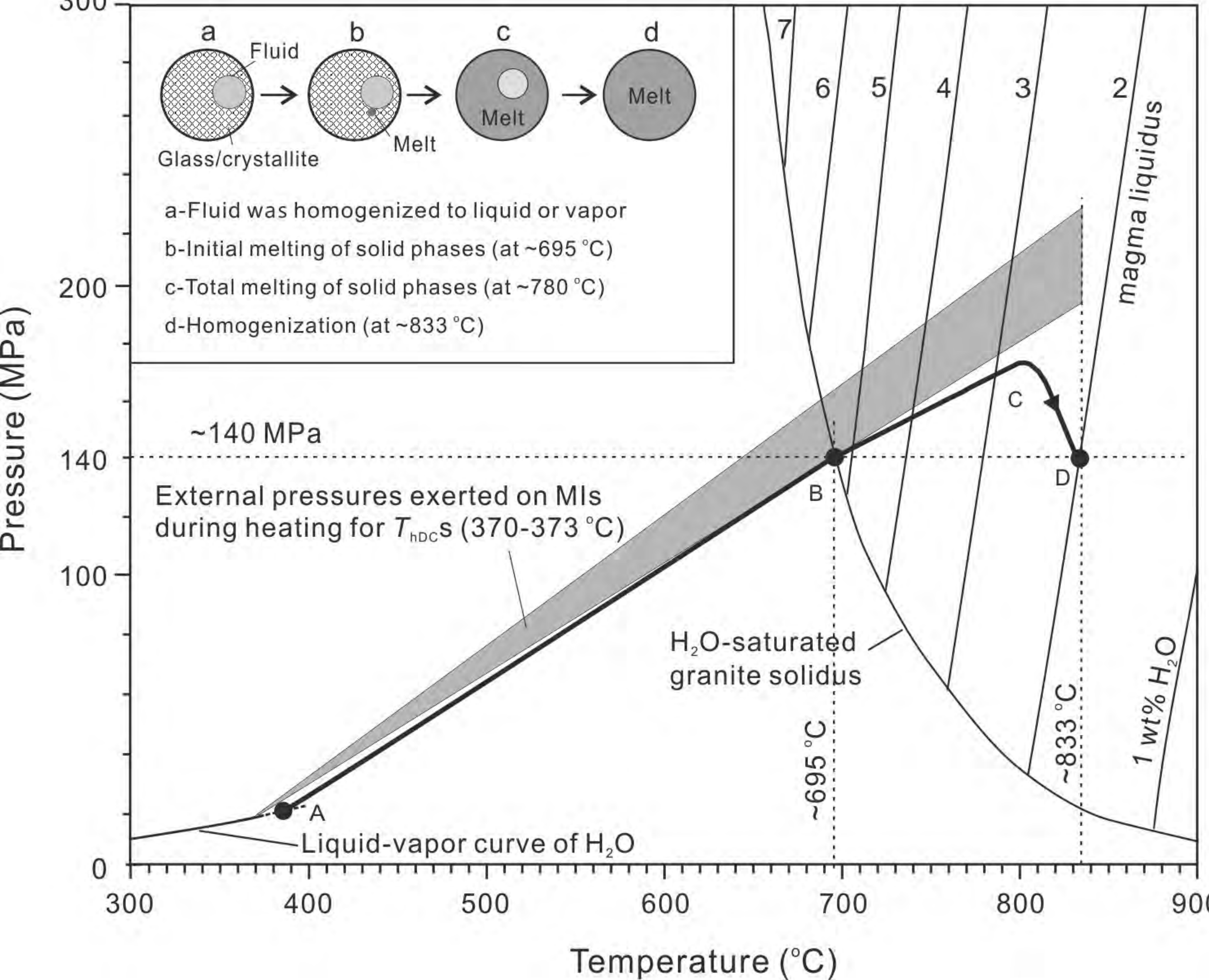
a
b
c
d
Fluid
Melt
Melt
Melt
Glass/crystallite
a-Fluid was homogenized to liquid or vapor
b-Initial melting of solid phases (at ~695 °C)
c-Total melting of solid phases (at ~780 °C)
d-Homogenization (at ~833 °C)
7
6
5
4
3
2
magma liquidus
~140 MPa
External pressures exerted on MIs
during heating for T_{hDC}s (370-373 °C)
A
B
C
D
H_2O-saturated
granite solidus
~695 °C
~833 °C
1 wt% H_2O
Liquid-vapor curve of H_2O
Pressure (MPa)
Temperature (°C)
300
200
140
100
0
300
400
500
600
700
800
900